Computers and Concrete, *Vol. 16, No.* 5 *(2015) 683-701*
DOI: http://dx.doi.org/10.12989/cac.2015.16.5.683

Modeling of reinforced concrete structural members for engineering purposes

Jacky Mazars[*1,2] and Stéphane Grange[1,2a]

[1]*University Grenoble Alpes, 3SR Laboratory, 38000 Grenoble, France*
[2]*CNRS, 3SR Laboratory, 38000 Grenoble, France*

(Received December 23, 2014, Revised August 1, 2015, Accepted November 1, 2015)

Abstract. When approached using nonlinear finite element (FE) techniques, structural analyses generate, for real RC structures, large complex numerical problems. Damage is a major part of concrete behavior, and the discretization technique is critical to limiting the size of the problem. Based on previous work, the μ *damage model* has been designed to activate the various damage effects correlated with monotonic and cyclic loading, including unilateral effects. Assumptions are formulated to simplify constitutive relationships while still allowing for a correct description of the main nonlinear effects. After presenting classical 2D finite element applications on structural elements, an enhanced simplified FE description including a damage description and based on the use of multi-fiber beam elements is provided. Improvements to this description are introduced both to prevent dependency on mesh size as damage evolves and to take into account specific phenomena (permanent strains and damping, steel-concrete debonding). Applications on RC structures subjected to cyclic loads are discussed, and results lead to justifying the various concepts and assumptions explained.

Keywords: concrete; damage models; cyclic loading; simplified modeling; cracking indicators

1. Introduction

For RC structures, structural analyses generate large complex numerical problems. The discretization technique proves to be a key step in controlling the size of such problems; moreover, damage remains a major component of concrete behavior (Simo and Ju 1987, Lubliner *et al.* 1989, La Borderie *et al*. 1994, Jirasek 2004).

Based on previous work Mazars (1986), Pontiroli *et al.* (2010), the μ *damage model* Mazars *et al*. (2015) offers the simplest and most complete set-up possible; it implies formulating the following set of main assumptions:

- Concrete behavior is considered as the combination of elasticity and damage;
- The damage description is assumed to be isotropic and directly affects the stiffness evolution of the material. Let $\mathbf{\Lambda}$ be the stiffness matrix of the original material, then the matrix for the damaged material is given by

*Corresponding author, Professor Emeritus, E-mail: jacky.mazars@3sr-grenoble.fr
[a]Associate Professor, E-mail: stephane.grange@3sr-grenoble.fr

http://www.techno-press.org/?journal=cac&subpage=8 ISSN: 1598-8198 (Print), 1598-818X (Online)

$$\underline{\underline{\underline{\Lambda}}}_d = \underline{\underline{\underline{\Lambda}}}(1-d) \tag{1}$$

- The stress tensor $\underline{\underline{\sigma}}$ –strain tensor $\underline{\underline{\varepsilon}}$ relationship is governed by

$$\underline{\underline{\sigma}} = \underline{\underline{\underline{\Lambda}}}_d : \underline{\underline{\varepsilon}} = \underline{\underline{\underline{\Lambda}}}(1-d) : \underline{\underline{\varepsilon}} \tag{2}$$

- As opposed to classical damage models, *d* denotes the effective damage. Classically speaking, damage is a variable that describes the micro-cracking state of the material. Moreover, *d* indicates the effect of damage on the stiffness activated by loading. In a cracked structure, *d* must serve to describe the effects of crack opening and crack closure.
- Two principal damage modes are considered (cracking and crushing) and subsequently associated with two thermodynamic variables Y_t and Y_c, which characterize the extreme loading state reached respectively in the tensile part and compressive part of the strain space.

A conventional FE technique is used to validate the relevance of the model. In order to reduce the size of nonlinear problems for real structures, a simplified FE description is considered for engineering purposes based on the use of multi-fiber elements for both beams and columns. Enhancements are introduced to limit the dependence on mesh size during damage evolution as well as to take specific phenomena into account, such as steel-concrete debonding, the hysteretic loop and permanent strains due to friction between crack lips and initial stresses. These concepts yield a tool as good as the conventional finite element calculation for accessing results, including at the local level (e.g., state of rebar deformation, average crack width) yet with better control over convergence problems and significant computational time savings.

2. Modeling context

2.1 Constitutive equations

A summary of the μ damage model is proposed below. For a more detailed presentation, see Mazars *et al.* (2015).

Like for a previous model Mazars (1986), let's consider the equivalent strain concept.

Below, we define ε_t and ε_c as the equivalent strain for cracking and crushing, respectively. (*ν is the Poisson ratio)*

$$\varepsilon_t = \frac{I_\varepsilon}{2(1-2\nu)} + \frac{\sqrt{J_\varepsilon}}{2(1+\nu)} \tag{3}$$

$$\varepsilon_c = \frac{I_\varepsilon}{5(1-2\nu)} + \frac{6\sqrt{J_\varepsilon}}{5(1+\nu)} \tag{4}$$

$$I_\varepsilon = \varepsilon_1 + \varepsilon_2 + \varepsilon_3 \quad \text{and} \quad J_\varepsilon = \frac{1}{2}[(\varepsilon_1-\varepsilon_2)^2 + (\varepsilon_2-\varepsilon_3)^2 + (\varepsilon_3-\varepsilon_1)^2] \tag{5}$$

Two independent loading surfaces are now associated

$$f_t = \varepsilon_t - Y_t \quad \text{and} \quad f_c = \varepsilon_c - Y_c \tag{6}$$

such that during gradual $Y_{t(c)}$ evolution, the identity $f_{t(c)}=0$ holds, else $f_{t(c)} < 0$.

Y_t and Y_c define the maximum values reached on the loading path

$$Y_t = Sup[\varepsilon_{0t}, max\,\varepsilon_t] \quad \text{and} \quad Y_c = Sup[\varepsilon_{0c}, max\,\varepsilon_c] \tag{7}$$

ε_{0t} and ε_{0c} are the initial thresholds of ε_t and ε_c respectively.

2.2 Damage evolutions

The effective damage d is directly correlated with the thermodynamic variables Y_t and Y_c through the driving variable Y,

i.e.

$$Y = rY_t + (1-r)Y_c, \qquad \text{with} \quad r = \frac{\sum < \bar{\sigma}_i >_+}{\sum |\bar{\sigma}_i|} \tag{8}$$

where r is the triaxiality factor (Lee and Fenves 1998), which evolves within the stress space from 0, for the compressive stress zone, to 1 for the tensile stress zone; $\bar{\underline{\underline{\sigma}}} = \frac{\underline{\underline{\sigma}}}{(1-d)} = \underline{\underline{\underline{\underline{\Lambda}}}} : \underline{\underline{\varepsilon}}$ is the "effective stress"; $< x >_+$ and $|x|$ denote the positive part and absolute value of x, respectively. Therefore, r is damage-independent and can be determined at each calculation step without iteration. As was the case with Mazars' model (1986), the damage evolution law is defined by

$$d = 1 - \frac{(1-A)Y_0}{Y} - A\,exp(-B(Y - Y_0)), \text{ where } \; Y_0 = r\,\varepsilon_{0t} + (1-r)\varepsilon_{0c} \tag{9}$$

Y_0 is the initial threshold for Y. Variables A and B determine the shape of the effective damage evolution laws and subsequent behavioral laws. [A, B] evolves from [At, Bt] for the "cracking" curves to [Ac, Bc] for the "crushing" curves. At, Bt, Ac, Bc are all material parameters directly identified from uniaxial experiments (tensile or flexural tests and uniaxial compression tests).

The proposal for A and B is as follows

$$\begin{gathered} A = A_t(2r^2(1-2k) - r(1-4k)) + A_c(2r^2 - 3r + 1) \\ B = r^{(r^2-2r+2)} B_t + (1 - r^{(r^2-2r+2)}) B_c \end{gathered} \tag{10}$$

When r = 0 (i.e., compressive stress domain), A=A_c and B=B_c; conversely, when r=1 (i.e., tensile stress domain), A=A_t and B=B_t. k is introduced to calibrate the asymptotic stress value at large displacements in shear (useful to describe concrete-rebar friction): k=A(r=0.5)/A_t ; a standard value for k is 0.7 (see Fig. 1).

It is straightforward to demonstrate that when r is a constant (i.e., radial path), compliance with thermodynamic principles (Lemaitre *et al.* 1990) is ensured. When r is a variable however, it has been shown that these principles are still being respected, even for complex loading situations.

2.3 Model responses

In the σ_3 = 0 plane, Fig. 1 displays the plots of both the damage initiation surface (d = 0) and

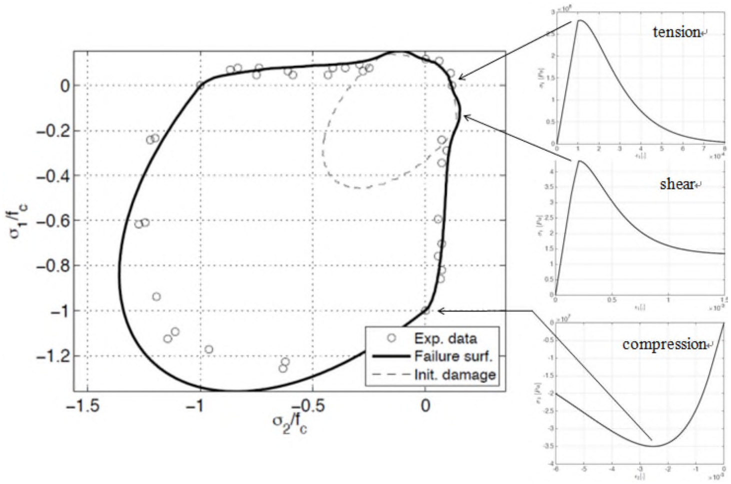

Fig. 1 Plane σ_3=0: plots of both, the damage initiation surface (dashed line) and the failure surface (strength envelope from different loading paths), compared to the experimental results provided by Kupfer *et al.* (1973)

the failure surface. The resulting plot corresponds to the maximum stress envelope (normalized by the compressive strength f_c), as obtained from curves at the prescribed $\sigma_1/\ \sigma_2$ ratios: three specific curves are shown in Fig. 1, tension (σ_2=0), shear (σ_2=-σ_1), and compression (σ_1=0). This figure also plots experimental data used for the failure surface and derived from several biaxial tests along various loading paths on an ordinary concrete specimen (Kupfer and Gurstle 1973). This model offers very good results, with just a few differences observed near the bisector in the bi-compression area.

2.4 1D version of the model

It was observed in Section 2.2 that the driven variable for *d* is *Y*. From Eq. (7) and for a uniaxial situation, it is derived that: $Y=Y_t$ for tension (r = 1), and $Y=Y_c$ for compression (r = 0).

From Eq. (2) and (8) therefore, two expressions are found to describe uniaxial behavior.

- For tension

$$\sigma = E(1-d_t)\varepsilon \quad \text{with} \quad d_t = 1-\frac{(1-A_t)Y_{0t}}{Y_t} - A_t \exp(-B_t(Y_t - Y_{0t})) \tag{11}$$

where Y_t = $Sup(\varepsilon_{ot},\ max\ -\varepsilon)$ and Y_{0t} = ε_{ot} = -σ_{0t}/E; for 1D calculations, it can be useful to use σ_{0t} as tension damage threshold;

- For compression

$$\sigma = E(1-d_c)\varepsilon \quad \text{with} \quad d_c = 1-\frac{(1-A_c)Y_{0c}}{Y_c} - A_c \exp(-B_c(Y_c - Y_{0c})) \tag{12}$$

where Y_c = $Sup(\varepsilon_{oc},\ max\ -\varepsilon)$ and Y_{0c} = ε_{oc} = - σ_{0c}/E; for 1D calculations, it can be useful to use σ_{0c} as compression damage threshold.

Fig. 2 shows the corresponding uniaxial response with a specific loading path, from OAB in

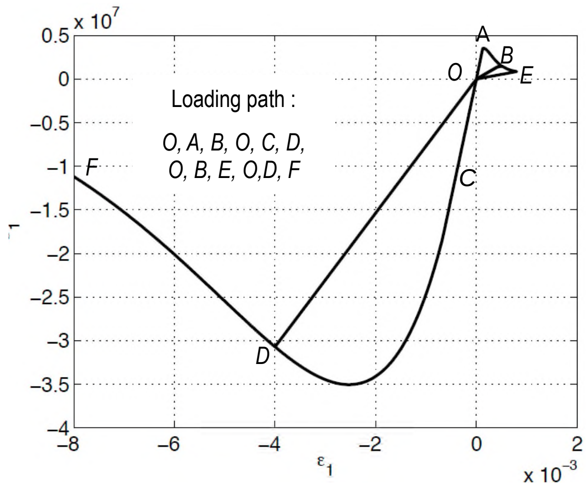

Fig. 2 Tension-compression loading path exhibiting the unilateral effect

tension to ODF in compression while highlighting the range of evolution in stiffness due to crack opening and closure (i.e., the unilateral effect).

We will demonstrate in the following discussion the relevance of this model in describing the behavior of reinforced concrete structural elements. On the basis of the same experiments on cyclic RC beams, two approaches, namely a 2D classical FE and a multi-fiber (MF) beam description, will be used and compared. From this comparison, enhancements will be proposed to improve the MF description in including an enhanced version of the 1D model.

3. 2D FE description for structural applications

The applications available using the μ model are primarily severe loadings on concrete structures. Among these applications, earthquakes are a key focus since they generate nonlinear cyclic loadings on structural elements. The strain rate is small enough to be neglected as an issue, unlike the case with blasts and shocks. The LMT Laboratory at ENS Cachan (France) conducted an experimental campaign on reinforced concrete (RC) beams in order to study the phenomena that play a major role in RC structural responses during an earthquake (Ragueneau *et al*. 2010, Crambuer *et al.* 2013). The phenomena of damage evolution during increased loading, unilateral effects and energy dissipation due to cyclic loads have all been analyzed. These results will serve for the subsequent applications.

3.1 Experimental program on a beam under cyclic loading

This entire campaign entailed various longitudinal reinforcement steel ratios, though this paper only considers the specimens reinforced with four 12-mm rebar (Fig. 3(a)). The concrete tested was a regular C30/37, whose characteristics are listed in Table 1.

The RC beams were designed for testing with a simple three-point bending set-up in a two-way vertical direction. A custom hinge device ensured a free-rotation condition at the end of the support beams. The specimens measured 1.65 m long by 0.22 m high by 0.15 m wide. The loading path

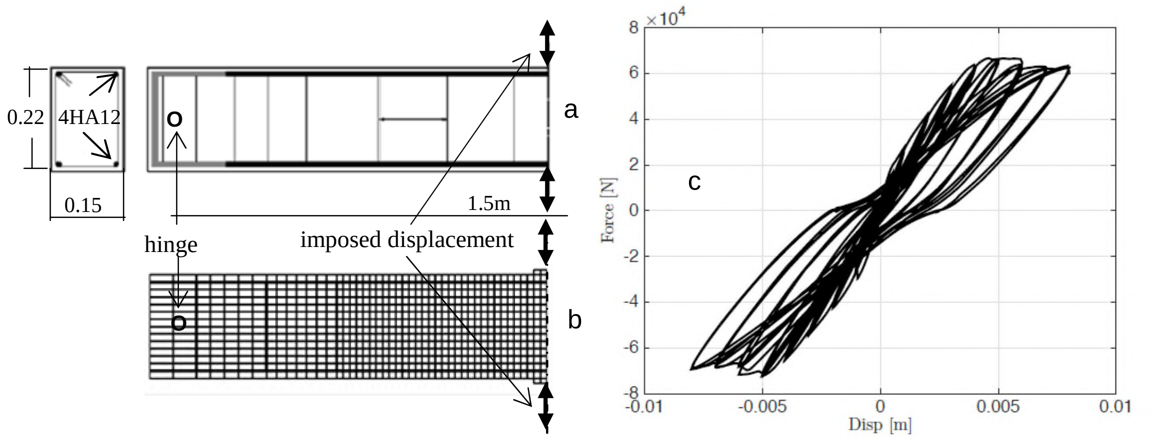

Fig. 3 Three-point bending tests: (a) specimen geometry and boundary conditions, (b) mesh used for calculations, (c) experimental results for the entire loading path

was displacement-controlled and included sets of 3 cycles with gradually increasing intensity (from ±0.5 mm to ±8 mm). Fig. 3(c) shows the force-displacement response of the beam for the full loading path; more specifically, it indicates: i) a gradual decrease in stiffness due to concrete damage during the first series of cycles, and ii) the appearance of rebar plasticity after the ±4 mm cycles and a continued predominance beyond this stage.

3.2 2D finite element descriptions

The calculations presented in this paper have been made on the platform ATLAS developed at 3SR Grenoble (Grange 2015a, b). The test specimen was modeled using Q4 (four nodes) elements under a plane stress assumption and bar elements for the rebar. The symmetry of the problem was introduced, and the mesh for the half-beam (711 nodes, 776 elements) was uniform over the central part of the beam; moreover, boundary conditions were defined so as to correctly represent the experimental test (Fig. 3(b)). The imposed displacement U_y was applied on both the upper and lower parts within the central section of the beam.

To avoid mesh sensitivity, the crack band approach based on the fracture energy concept was introduced into this application (Bazant and Oh 1983). The definition of G_f was derived according to Planas and Elices (1992) and Bazant (2002), meaning that in the central part of the beam (i.e., where damage and plasticity are concentrated), element size is consistent with the crack band width h

$$h = \frac{2G_f}{f_t^2}\left(\frac{1}{E} - \frac{1}{E_t}\right)^{-1} \tag{13}$$

with E_t being the post-peak tangent stiffness for an equivalent triangular shape of the σ–ε curve. The model parameter values used were selected in accordance with the data provided in Table 1.

Regarding the rebar, bar elements have been used, in compliance with a simple elasto-perfectly plastic model, whose parameter values are given in Table 1.

Table 1 RC bending tests: experimental data and material specifications for the FE calculations

Experimental data				Concrete model parameters								
Steel		Concrete										
E GPa	*fe* MPa	*E* GPa	*fc* MPa	*E* GPa	ν	ε_{t0}	ε_{c0}	*At*	*Bt*	*Ac*	*Bc*	*Gf* N/m
205	500	28	35	28	0.2	1e-4	3.6e-4	0.8	7000	1.25	395	30

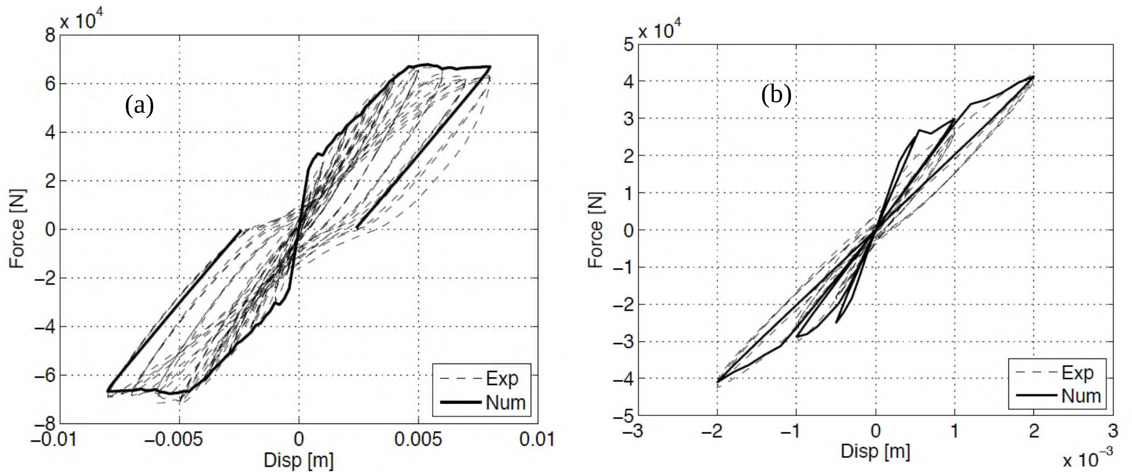

Fig. 4 Bending test on RC beams as an experiment-calculation comparison: (a) comparison of the envelope of the total experimental response with a calculation driven without any cycle; (b) total path up to ±2 mm

3.2.1 Overall results

A number of situations have been modeled herein. For example, Fig. 4(a) compares, for the total loading path, the load-displacement calculation curve, performed without any cycle, with the envelope for the entire set of experimental curves.

Fig. 4(b) then compares the curve resulting from the simulations with experimental points for the same loading path up to ±2 mm. These comparisons indicate a very good level of agreement.

From these results, it can be concluded that stiffness recovery, as depicted by the μ model, accurately reproduces the experimental results. Let's also point out however that introducing hysteretic loops and permanent strains in the concrete behavior could improve the result in Fig. 4(b).

3.2.2 Local results

Such a modeling approach serves to access the local information that indicates what is taking place inside the damaged areas in both the concrete and rebar. Fig. 5 shows, at a given stage of the loading (-3 mm), the damage field on the lateral beam surface predicted by calculation after a series of cycles extending to ±3 mm (the colored marks indicate where $0.8 < d < 1$). During a cyclic loading, the effective damage d evolves until reaching a maximum value in one direction; due to a change in the triaxiality factor r from 1 to 0, this maximum value vanishes once the local stress has been reversed. It can be observed that the effective damage d serves as an indicator of a crack opening stage. A good level of agreement has been found by means of digital image

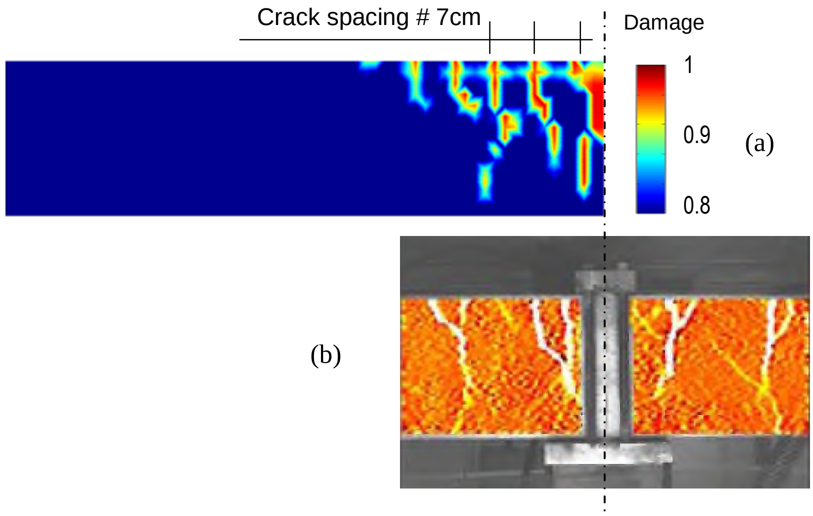

Fig. 5 RC bending beam, (a) effective damage used as a crack opening indicator (d>0.8) after cycles up to ±3 mm, (b) cracks observed through digital image correlation with a deflection of -3 mm

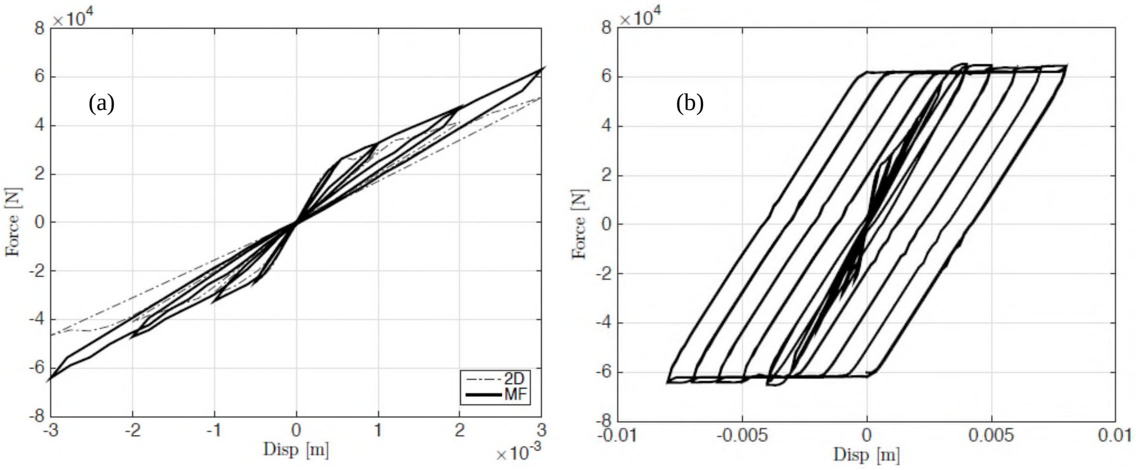

Fig. 6 Flaws in the response of the classical multi-fiber beam description for the 3-point bending RC beam: (a) overestimation of the behavior with the same parameters as those used in the FE description; (b) cyclic response of the multi-fiber beam description at large deformation, in exhibiting great discrepancy with the experimental results shown in Fig. 3(c)

correlation analysis during the experiments (Ragueneau *et al.* 2010).

These results reveal an efficient model and one that has proven to be robust and effective in describing cyclic behavior. The μ model is thus a good candidate for solving seismic problems.

4. Simplified modeling for structural applications

To decrease the number of degrees of freedom, 3*D* Timoshenko multi-fiber beam elements have been used to treat the same kind of problem (Kotronis and Mazars 2005). Based on a 1D model, nonlinear fibers were associated with the μ damage model for concrete as well as with an elastic-perfectly plastic model for rebar. This beam description generates kinematic constraints to ensure respecting both the continuity of displacement between two elements and all plane sections. The concrete section of the multi-fiber beam is a matrix containing 5×7 fibers. Differently-sized beam elements are introduced into the various calculations that follow, with boundary conditions the same as those in Fig. 3.

4.1 Multi-fiber beam: flaws in the description

4.1.1 Flaws resulting from the choice of material parameters

By relying on the same parameters as those used for the finite element calculation above (Table 1), it can be determined that:

- The description of cyclic loading, when rebar remains elastic, yields a force overestimation (Fig. 6(a)).
- The description of cyclic loading, when rebar plasticity is activated, overestimates the plastic strain of reinforcement (Fig. 6(b)) when compared with experimental results (Fig. 3(c)).

4.1.2 Multi-fiber beams and strain localization

Concrete exhibits softening, which in turn leads to strain localization and results that depend on element size. Strain localization is a major concern in maintaining the objectivity of finite element calculations. This problem is well known in classical 2D-3D calculations, for which two principal treatment options are available: i) the solution presented above with material parameters adjusted to suit element size (Hillerborg *et al.* 1976), and ii) implementation of regularization methods such as non-local methods (Pijaudier and Bazant 1987). Such a problem has never before been studied in the context of a multi-fiber beam description.

To illustrate this point in using multi-fiber beam elements and in considering the beam presented Fig. 3, we performed calculations for each of the three loading types (i.e., tension, 3-point bending, 4-point bending). These results are summarized in Table 2 and suggest that localization only appears with tensile loading.

More generally speaking, a fiber beam description contains localization if the behavior of the beam element displays softening. Localization is thus present for:

- a plain concrete element, regardless of its loading (tension or bending);
- a RC element if the loading is uniaxial and tensile (localization appears once the concrete has failed);
- a RC element in bending when the reinforcement ratio is less than a minimum value, referred to as the fragility ratio (see Eurocode 2 2004).

For other reinforcement ratio values, if bending is dominant (should bending and tension be combined), no localization is present.

Hillerborg stipulated that the energy dissipated at failure in a unit concrete volume must be equal to the fracture energy. In the presence of localization, the control of result objectivity would then be the same as for classical 2D-3D FE calculations. Localization takes place within a band of elements, and the material parameters must be calibrated with the size *h* of these elements (Fig. 7(a). In the absence of localization, the damage-cracking processes for one crack are distributed on both sides of the crack over a volume defined by the distance s_c between two cracks (Fig. 7(b)). Therefore, the concept of crack band cannot be applied here. The calculation must be calibrated so that the fracture energy is consumed in a s_c wide area, leading us to write

Table 2 Multi-fiber description: various types of loadings applied on the same RC element and the corresponding damage fields, therefore proving that localization is not always systematic

Type of loading	Overall behavior (load-displacement)	Damage contour (at a given loading)	Type of response
Tensile loading (tie) 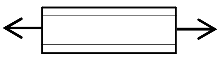	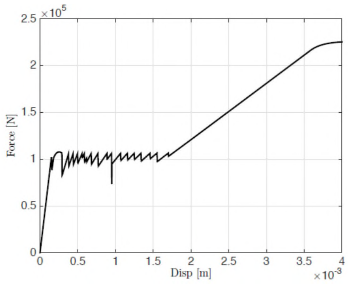	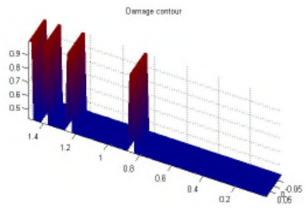	Strain is localized
Four-point bending 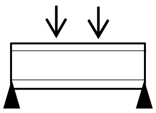	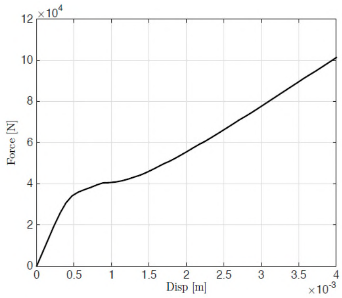	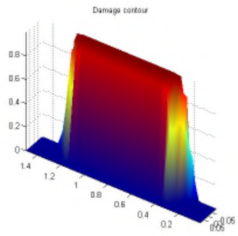	Strain is distributed
Three-point bending 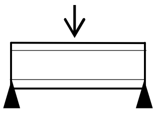	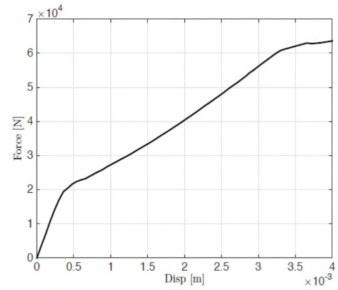	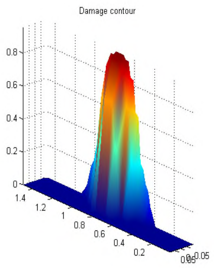	Strain is distributed

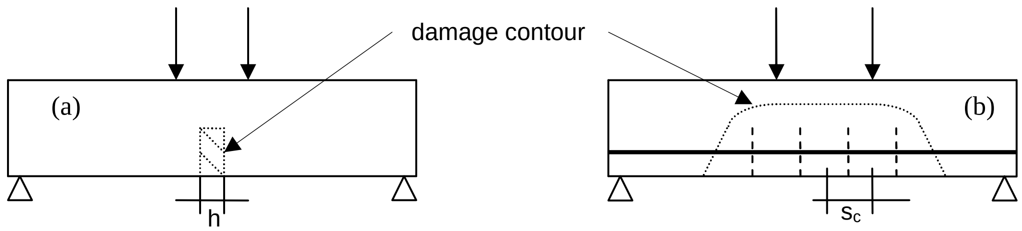

Fig. 7 Localization processes in a multi-fiber beam description, (a) plain concrete: damage is localized in a band of elements (size h); and (b) reinforced concrete: damage is distributed along the cracking zone (s_c is the crack spacing)

$$G_f = s_c \int \sigma d\varepsilon \tag{14}$$

with

$$s_c \int_{MF} \sigma d\varepsilon = h \int_{FE} \sigma d\varepsilon \tag{15}$$

The material parameters must then be calibrated in relation to this distance (s_c).

4.2 Multi-fiber description with enhancements and use of adapted parameters

4.2.1 Cracking stage

As illustrated above, application of the Hillerborg method can no longer be based on beam element length, like for the FE description, but instead on the spacing between cracks s_c. Hence, s_c must be known in advance from previous calculation, experimental observation or from rules proposed in design codes. In order to demonstrate the relevance of this approach, in the present case, s_c has been chosen based on results of the previous FE calculation conducted on the same beam (s_c =0.07 m, see Fig. 5). The tensile behavior was calibrated in accordance with Eq. (15). This step can be performed from the μ model by adjusting the post-peak curve parameters according to the *At* and *Bt* values (Eq. (11)). The choice for the beam considered herein is *At*=1 and *Bt*=8000, instead of the corresponding values given in Table 1 for the 2D FE calculations.

On the basis of these findings, it can be concluded that:

- The overestimation previously described in the cracking phase disappears (Fig. 8(a));
- This result is clearly insensitive to a change in mesh size (Fig. 8(b)), thus demonstrating that this procedure leads to an objective calculation.

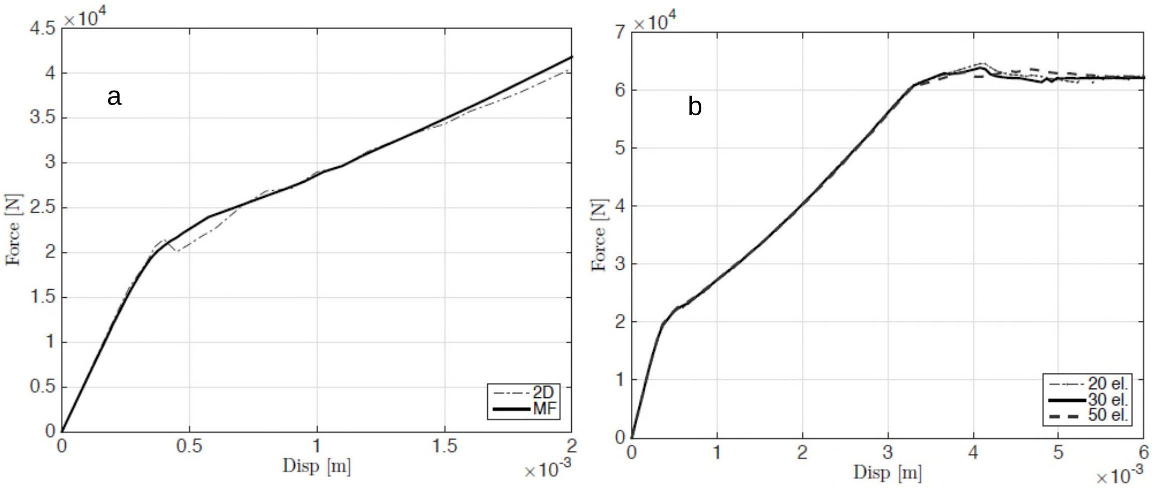

Fig. 8 Calibration of the multi-fiber (MF) description model parameters to show: (a) a comparison of results from the previous 2D finite element calculation with those of the MF beam using parameters derived from crack spacing considerations; and (b) independence of the MF result with respect to mesh size

4.2.2 Cyclic behavior

In a Timoshenko beam, the behavior of each fiber is uniaxial. To improve replication of the concrete cyclic behavior, we have upgraded the 1D version of the μ model presented in Section 2.4 by introducing a hysteretic loop as well as the permanent strain generated from friction between the crack lips and the release of initial stresses.

Hysteretic loop

During unloading or reloading, the hysteretic loop is described using a specific partition of the total strain, i.e.: $\sigma_t = \sigma + \sigma_d$, where $\sigma = E(1-d_i)\varepsilon$ and, as shown in (Pontiroli *et al*. 2010), the damping stress (σ_d) is given by

$$\sigma_d = (\beta_1 + \beta_2 d_i) E(1-d_i)\varepsilon . f_i(\varepsilon).sign(\dot{\varepsilon}) \quad (i=t,c) \tag{16}$$

β_2 and β_1 are related to damping, respectively with and without damage. The sign is - for unloading ($\dot{\varepsilon} < 0$) and + for reloading ($\dot{\varepsilon} > 0$). d_i is used to distinguish the damage value in tension (d_t) from that in compression (d_c); moreover, $f_i(\varepsilon)$ is associated with d_i and its driven variable Y_i; it also provides both the shape and size of the loop

$$f_i(\varepsilon) = 4\frac{\varepsilon^2}{Y_i^2}(\varepsilon - Y_i) \quad (i=t,c) \tag{17}$$

Permanent strains

This principle consists of considering a shift (ε_{ft}, σ_{ft}) in the $\sigma-\varepsilon$ axis, such that

$$(\sigma - \sigma_{ft}) = E(1-d_i)(\varepsilon - \varepsilon_{ft}) \tag{18}$$

Assuming the same concurrent point (ε_{fc}, σ_{fc}) for elastic unloading in compression, we obtain

$$\sigma_{ft} = E(1-d_c)(\varepsilon_{ft} - \varepsilon_{fc}) + \sigma_{fc} \tag{19}$$

ε_{ft} depends on the damage value in compression; it equals ε_{ft0} if d_c=0. Assuming a constant value regardless of d_c for the stress at crack-closure ($\sigma_{ft} = E\varepsilon_{ft0}$), from (19) it can be deduced that

$$\varepsilon_{ft} = \frac{\varepsilon_{ft0} - \varepsilon_{fc} d_c}{1-d_c} \tag{20}$$

ε_{ft0} and ε_{fc} are material parameters.

The resulting $\sigma-\varepsilon$ curve is shown in Fig. 9(b), and the corresponding material parameters are listed in Table 3. The curve improvement only modified the unloading and reloading responses. For a monotonic loading in tension or compression, the σ–ε curve remains exactly the same as before. Let's note (Fig. 9(b)) that permanent strain is created whenever damage evolves in tension but vanishes during unloading. Conversely, the permanent strain created in compression is definitive.

Table 3 Concrete material parameters for enhanced MF calculations

E GPa	σ_{0t} MPa	*Gf* N/m	*At*	*Bt*	σ_{0c} MPa	*Ac*	*Bc*	ε_{ft0}	ε_{fc}	β_1	β_2
28	2.8	30	1	8000	-10	1.25	395	-0.35e-4	4e-4	0.05	0.20

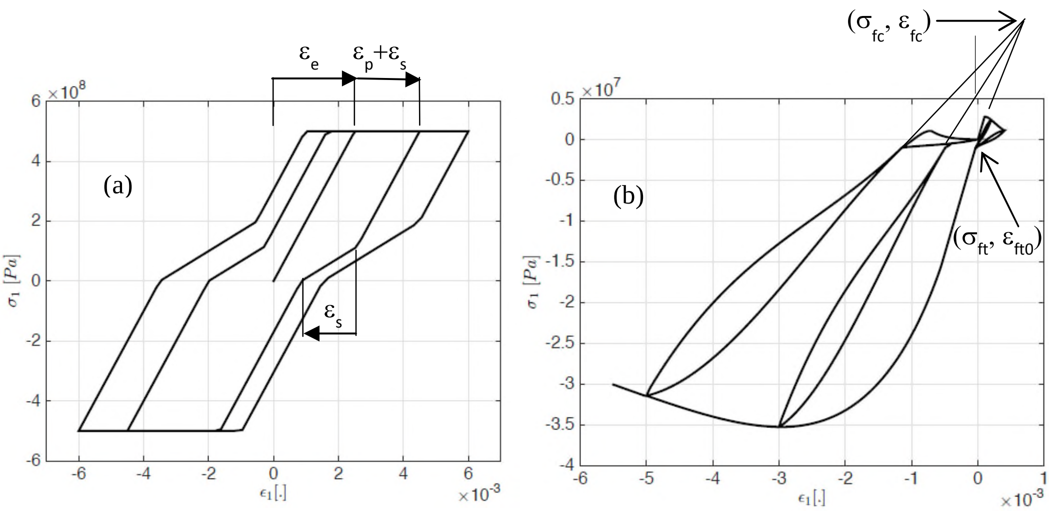

Fig. 9 Enhanced MF beam: (a) rebar-concrete bond curve obtained by introducing a sliding stage into the global steel fiber behavior, and (b) concrete curve including hysteretic loops and permanent strains

4.2.3 Multi-fiber beams and the steel-concrete bond

It is widely acknowledged that debonding between concrete and rebar occurs at large deformations. This phenomenon is especially sensitive whenever cracks open and steel yields. In a fiber beam description, given that no interaction is taking place between the fibers except at their ends and that the damage-fracture processes are distributed, debonding cannot be reproduced. This point leads to overestimating the plastic strain, as observed in Fig. 5(b).

As proposed by various authors, Richard *et al.* (2011), Wang *et al.* (2004), one way to introduce bond degradation and the relative sliding of rebar over concrete in a multi-fiber beam description is to split the total strain in the steel fiber into two parts: a first part associated with the proper strain of the steel (ε_e+ε_p), and the second part related to the sliding strain (ε_s) occurring at the steel/concrete interface

$$\varepsilon = \varepsilon_e + \varepsilon_p + \varepsilon_s \tag{21}$$

ε_e, ε_p, and ε_s are the elastic strain (ε_e=σ/E), plastic strain and sliding strain, respectively. Plastic strain depends on the selected elasto-plastic model. For a perfectly plastic model, the tensile response is

$$\sigma = \varepsilon_e E \text{ if } \varepsilon_p = 0, \text{ and } \sigma = f_e \text{ if } \varepsilon_p > 0 \tag{22}$$

Braga *et al.* (2012) proposed a modified steel bar model to account for bond slips in considering a nonlinear monotonic relationship for sliding. In order to minimize computational

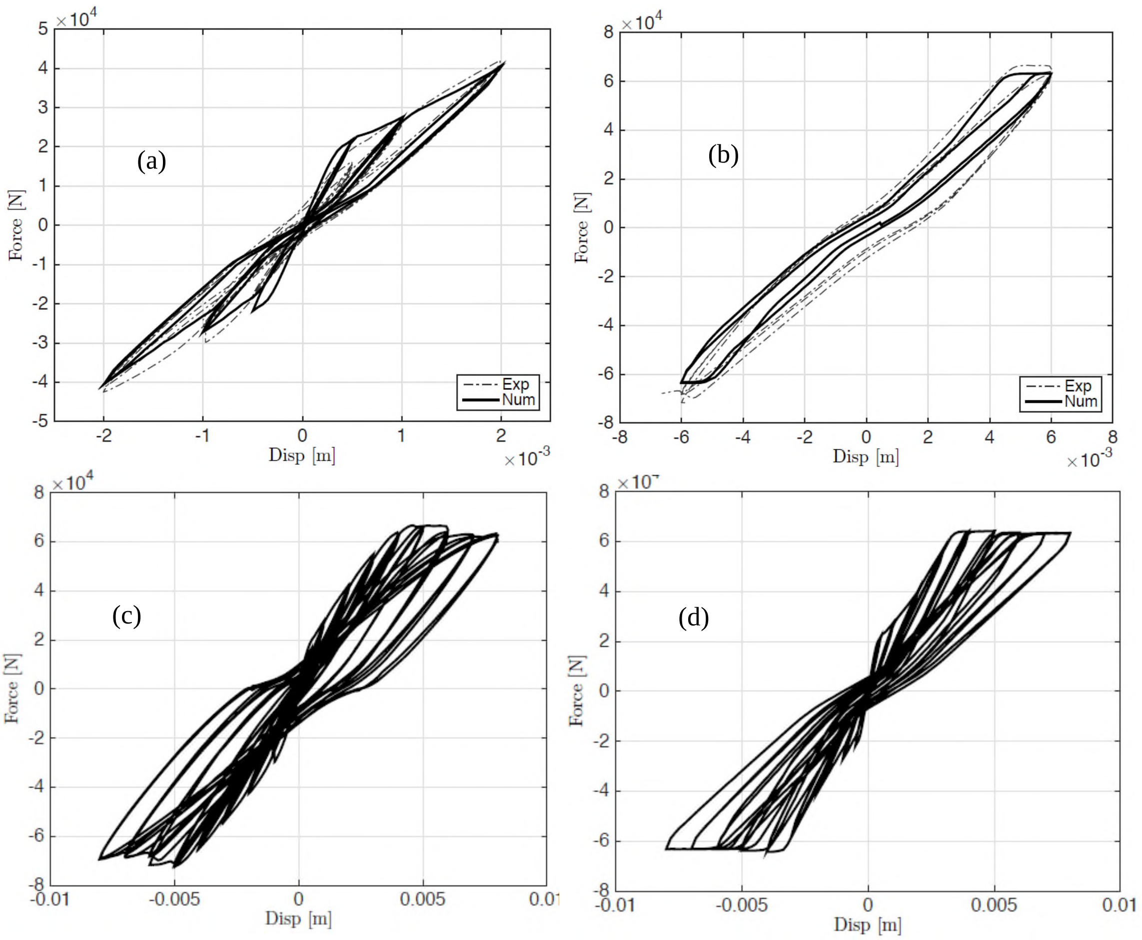

Fig. 10 Enhanced MF beam cyclic response: (a) experiment-calculation comparison up to ±2 mm, (b) comparison for a set of 3 cycles at ±6 mm, and a global cyclic loading path, with experiment (c), calculation (d)

effort, the present proposal is based on the following assumptions:

- Sliding strain evolves from a threshold and, assuming that the main sliding evolution occurs when plasticity is activated, this threshold is assumed to be the plastic threshold.
- A linear link exists between plastic strain and sliding deformation.

From these assumptions, the proposed sliding strain is

$$\varepsilon_s = \kappa\varepsilon_p \text{ if } \varepsilon_p > 0, \text{ and } \varepsilon_s = 0 \text{ otherwise} \tag{23}$$

For a cyclic loading, as the tensile load decreases (unloading), two stages appear: 1) a partial recovery of ε_e; and 2) from a given stage to zero stress, ε_s gradually vanishes and both ε_e and ε_s reach 0 when the strain rate sign changes. Then in continuing loading, as the load moves to compression, assuming that no sliding is possible when cracks are closed, ε_s=0 and (as shown in Fig. 9(a)) the sliding strain gradually reappears upon reloading in tension up to its previous value and then increases with ε_p.

4.2.4 Results obtained with these enhancements

With this new behavior and the material parameters given Table 3, the RC beam response is presented Fig. 10. This figure includes comparison experiment-calculation for three different loading paths:

- a cyclic path during the cracking stage to up ±2 mm Fig. 10(a);
- a cyclic path of 3 cycles at ±5 mm for which steel plasticity and rebar-concrete debonding are activated Fig. 10(b);
- the total path up to ±8 mm Fig. 10(c), (d).

A very accurate description of the experimental response can indeed be observed.

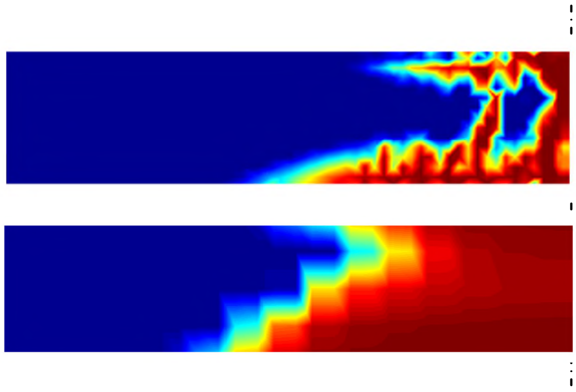

(a)

(b)

Fig. 11 Cracking fields in a RC beam at -3 mm after a loading path up to ±3 mm: (a) damage field from a 2D FE calculation, and (b) damage field from a multi-fiber beam calculation

4.3 Multi-fiber beam description and cracking indicators

Once improved, a multi-fiber beam description can also provide local information relative to cracking. Fig. 11 shows, for a given stage of loading (-3 mm after a global loading path up to ±3 mm), a comparison between the damage field obtained by the 2D FE description, which highlights crack locations, and the damage field obtained by the enhanced MF description presented above which is a distributed field. A good level of consistency can be observed between both.

Furthermore, a set of crack opening indicators can be derived. As mentioned in Section 4.1.3, an accurate description of the cracking phase is obtained by introducing crack spacing. Knowing such data ahead of time can pose a problem however. Experimental values (whether physical or numerical) may be used, or else one can rely on the set of rules proposed in design codes Eurocode 2 (2004), Model Code (2010). Given this knowledge, the calculation allows accessing a mean crack opening value.

It is generally considered that this opening appears beyond the peak stress f_t (Fig. 13(b)). For a length s_c equal to the distance between cracks, the crack opening w_c is therefore expressed as

$$w_c = s_c\,(\varepsilon - \varepsilon_{t0}) \quad \text{(where } \varepsilon_{t0} \text{ is the peak strain)} \tag{24}$$

Within the framework of the French national research program CEOS.fr (Mazars and Coste 2014), tests have been carried out on large beams in 4-point bending (length=6.1 m, width=1.6 m, height=0.8 m, see Fig. 12). During these tests, cracking was analyzed using digital image

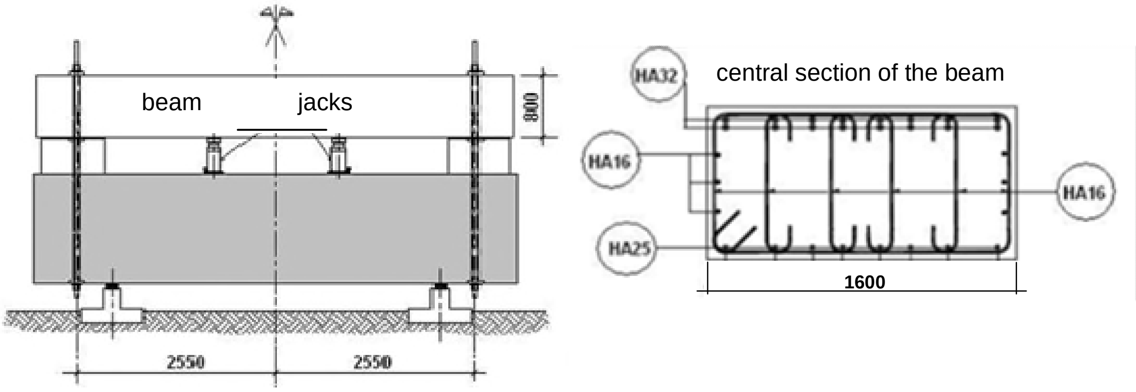

Fig. 12 CEOS.fr experiments on large 4-point bending RC beams: (a) test device system, and (b) reinforcement pattern for the RL6 beam (dimensions in mm)

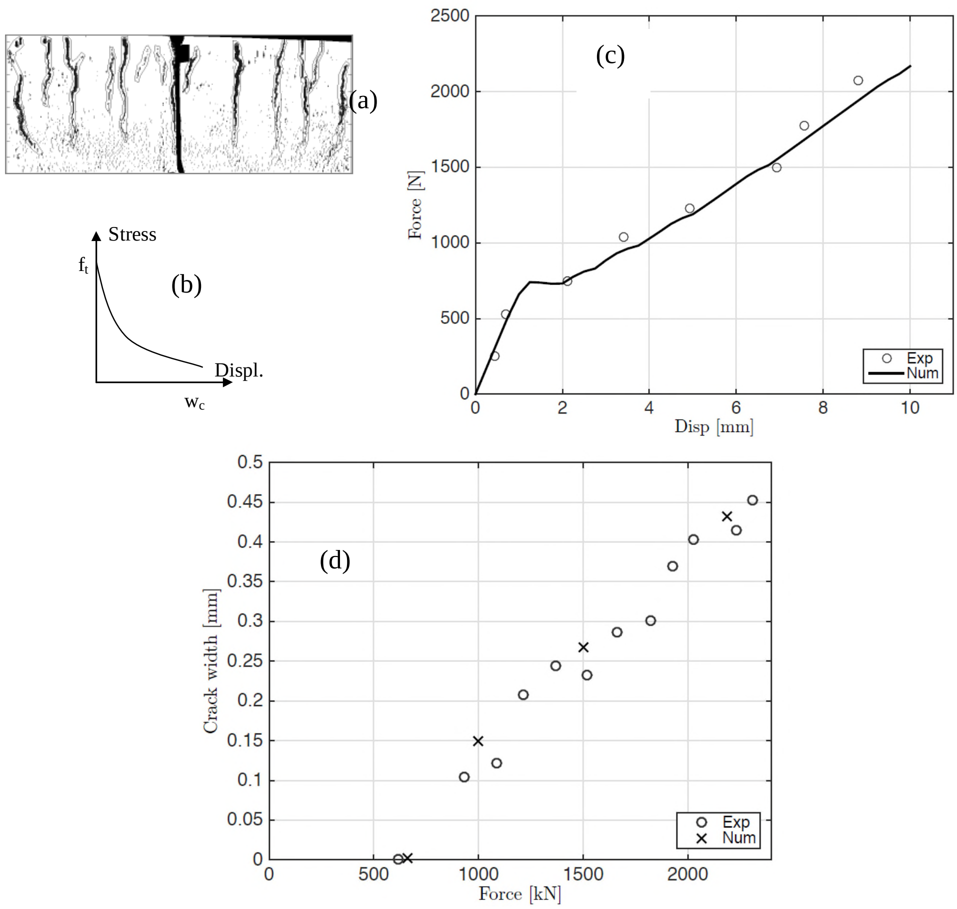

Fig. 13 Four-point RC bending tests, (a) crack pattern measured from the digital image correlation analysis within the central zone of the beam (mean spacing = 0.206 m), (b) the stress-crack opening curve, (c) load-displacement response, and (d) crack width (mean value at the upper reinforcement layer) vs. applied load

Table 4 Four-point RC bending tests (RL6): Experimental data and material specifications

Experimental data					Concrete model parameters						
Steel	Concrete										
E (GPa)	*E* (GPa)	*ft* (MPa)	*Gf* (N/m)	*fc* (MPa)	*E* (GPa)	σ_{0t} (MPa)	*At*	*Bt*	σ_{0c} (MPa)	*Ac*	*Bc*
195	40	4.67	75	63.75	40	4.67	1	11500	-150	1.5	355

correlation Fig. 13(a), thus providing access to both the spacing and crack width in the pure bending zone (Rospars and Chauvel 2014).

Just like for the previous beam, this calculation has been performed using a multi-fiber beam description. The concrete cross-section is a matrix composed of 8×16 fibers; in addition, the pure bending zone (1.6 m) has been divided into 10 elements.

The Hillerborg method was implemented on the basis of crack spacing obtained on the RL6 test beam (mean value: 0.206 m), and this calculation was conducted using model parameters estimated from the material properties (Table 4).

Fig. 13(c) reveals the good correlation for global behavior (load-displacement). From Eq. (25), the average crack width is determined at the level of the upper reinforcement, and the high quality of the results obtained Fig. 13(d) is now apparent.

5. Conclusions

Based on the finding that damage is a major part of concrete behavior, the first part of this paper presented a new damage model (the "μ model") relying on the principles of isotropic damage mechanics. Two thermodynamic variables were defined in order to describe, within a 3D formulation, the unilateral behavior of concrete (i.e., crack opening and closure), which is essential for cyclic loadings and particularly the seismic response of concrete structures. Furthermore, the mate-rial parameters are easy to identify from individual tensile and compressive tests alone. A series of applications using classical FE calculations has yielded satisfactory results when compared to experimental results, thus attesting to the model's effectiveness.

To reduce the size of nonlinear problems for real structures, a simplified FE description has been considered for engineering purposes; it is based on the use of multi-fiber beam elements for beams as well as columns. Enhancements were included both to avoid dependence on mesh size as damage evolves and to take into account specific phenomena such as steel-concrete debonding, hysteretic loops and permanent strains on the concrete.

These concepts have helped build a tool for accessing results, along with a conventional finite element calculation. Results include the local level (e.g., state of rebar deformation, average crack width) though with a better control of convergence problems and considerable computational time savings.

Along these same lines, other improvements are ongoing and include:

- for the 3D and 1D μ model, a description of the strain rate effect via a variation in the initial threshold of the driving damage variable, so as to model high-velocity loading effects;
- for simplified approaches: i) based on the enhanced modeling presented herein, the deve-lopment of equivalent lattice modeling for RC walls; and ii) the introduction of section warping to treat torsion and shear effects (Capdevielle *et al.* 2015).

In conclusion, this model and the strategy proposed to achieve simplified modeling have provided a useful tool for engineering applications; moreover, this tool can cover a wide array of problems, whether monotonic or cyclic, encompassing quasi-static and dynamic loadings.

Acknowledgments

The authors would like to thank the French national program CEOS.fr for its financial support and Prof. F. Ragueneau (LMT, ENS Cachan) in particular for his valuable assistance in providing the experimental results.

References

Bazant, Z.P. and Oh, B.H. (1983), "Crack band theory for fracture of concrete", *Mater. Struct.*, **16**(3), 155-177.

Bazant, Z.P. (2002), "Concrete fracture models: testing and practice", *Eng. Fract. Mech.*, **69**, 165-205.

Braga, F., Gigliotti, R., Laterza, M., D'Amato, M. and Kunnath, S. (2012), "Modified steel bar model incorporating bondslip for seismic assessment of concrete structures", *J. Struct. Eng.*, ASCE, **138**(11), 1342-1350

Capdevielle, S., Grange, S., Dufour, F. and Desprez, C. (2015), "A multifiber beam model coupling torsional warping and damage for reinforced concrete structures", *Eur. J. Envir. Civil Eng.*, doi:10.1080/19648189.2015.1084384. (accepted for publication)

Crambuer, R.B., Richard, B., Ile, F. and Ragueneau, F. (2013), "Experimental characterization and modeling of energy dissipation in reinforced concrete beams subjected to cyclic loading", *Eng. Struct.*, **56**(0), 919-934.

EN1992-2 and Eurocode 2 (2004), Design of concrete structures.

Hillerborg, A., Modeer, M. and Peterssonn, P.E. (1976), "Analysis of crack formation and growth in concrete by means of fracture mechanics and finite elements", *Cement Concrete Res.*, **6**, 773-782.

Jirásek, M. (2004), "Non-local damage mechanics with application to concrete", *French J. Civil Eng.*, **8**, 683-707.

Kotronis, P. and Mazars, J. (2005), "Simplified modelling strategies to simulate the dynamic behavior of R/C walls", *J. Earthq. Eng.*, **9**(2), 285-306.

Kupfer, H.B. and Gerstle, K.H. (1973), "Behavior of concrete under biaxial stresses", *J. Eng. Mech.*, **99**(4), 853-866.

Grange, S. (2015a), ATLAS - A Tool and Language for Simplified Structural Solution Strategy - Internal report, 3SR-Lab, Grenoble.

Grange, S. (2015b), "Modèles multi-échelles et algorithmes pour les simulations dynamiques: application à la vulnérabilité sismique des structures", Habilitation à diriger des recherches, Université de Grenoble-Alpes.

La Borderie, C., Mazars, J. and Pijaudier-Cabot, G. (1992), "Response of plain and reinforced concrete structures under cyclic loadings", A.C.I Special Publication, Eds. W. Gerstle and Z.P. Bazant, SP-134, 147-172.

Lee, J. and Fenves, G.L. (1998), "Plastic-damage model for cyclic loading of concrete structures", *J. Eng. Mech.*, **124**, 892.

Lemaitre, J. and Chaboche, J.L. (1990), *Mechanics of Solid Mater.*, Cambridge University Press.

Lubliner, J., Oliver, J., Oller, S. and Onate, E. (1989), "A plastic-damage model for concrete", *Int. J. Solid. Struct.*, **25**(3), 299-326.

Mazars, J. (1986), "A description of micro and macroscale damage of concrete structure", *Eng. Fract.*

Mech., **25**, 729-737.

Mazars, J. and Coste, J.F. (2014), "CEOS.fr National Project : behaviour and assessment of special structures in relation with shrinkage and creep", The French Technology of Concrete CEB-Fib, Mumbai.

Mazars, J., Hamon, F. and Grange, S. (2015), "A new 3D damage model for concrete under monotonic, cyclic and dynamic loading", *Mater. Struct.*, **48**, 3779-3793.

MC2010 Model Code (2010), fib Bulletin, Final Draft (2011).

Pijaudier-Cabot, G. and Bazant, Z.P. (1987), "Nonlocal damage theory", *J. Eng. Mech*., ASCE, **113**(10), 1512-1533.

Planas, J., Elices, M. and Guinea, G.V. (1992), "Measurement of the fracture energy using three-point bend tests: Part 2, influence of bulk energy dissipation", *Mater. Struct.*, **25**, 305-316.

Pontiroli, C., Rouquand, A. and Mazars, J. (2010), "Predicting concrete behaviour from quasi-static loading to hypervelocity impact", *Eur. J. Envir. Civil Eng*., **14(**6-7), 703-727.

Ragueneau, F., Lebon, G. and Delaplace, A. (2010), "Analyse expérimentale du comportement cyclique de poutres en béton armé", LMT Internal report, October.

Richard, B., Ragueneau, F., Lucas, A. and Crémona, C. (2011), "A multi-fiber approach for modelling corroded reinforced concrete structures", *Eur. J. Mech A-Solid*., **30**, 950-961.

Simo, J. and Ju, J. (1987), "Strain- and stress-based continuum damage models-I formulation", *Int. J. Solid. Struct.*, **23**, 821-840.

Rospars, C. and Chauvel, D. (2014), "CEOS.fr experimental programme and reference specimen tests results", *Eur. J. Envir. Civil Eng..*, **18**(7-8), 738-753.

Wang, X. and Liu, X. (2004), "Modeling bond strength of corroded reinforcement without stirrups", *Cement Concrete Res*., **34**, 1331-1339.

AW